International Journal of Heat and Mass Transfer 52 (2009) 1254–1267

Contents lists available at ScienceDirect

International Journal of Heat and Mass Transfer

journal homepage: www.elsevier.com/locate/ijhmt

Jet-array impingement heat transfer in a concentric annular channel with rotating inner cylinder

Shyy Woei Chang [a,*], Tsun Lirng Yang [b], Dar-Wei Shih [c]

[a] Thermal Fluids Laboratory, National Kaohsiung Marine University, No. 142, Haijhuan Road, Nanzih District, Kaohsiung City 81143, Taiwan, ROC
[b] Department of Marine Engineering, National Kaohsiung Marine University, No. 142, Haijhuan Road, Nanzih District, Kaohsiung City 81143, Taiwan, ROC
[c] Marine Engineering, National Kaohsiung Marine University, No. 142, Haijhuan Road, Nanzih District, Kaohsiung City 81143, Taiwan, ROC

ARTICLE INFO

Article history:
Received 28 April 2008
Received in revised form 22 August 2008
Available online 20 October 2008

Keywords:
Rotating jet-array impingement
Taylor–Couette–Poiseuille flow
Cooling electric rotor machine

ABSTRACT

As a new cooling scheme for electric rotor machines, the impinging jets issued from the armature onto the stator with the spent flows directed toward two annular exits at both ends can convect the Joule heat out of the rotor machinery effectively. An experimental study is accordingly devised to investigate the heat transfer performances over the outer cylinder of a concentric annulus with an impinging jet-array issued from the rotating inner cylinder. Intermittencies of impinging jets and spent flows in the Taylor–Couette–Poiseuille annular flow feature the dominant flow physics that affect the heat transfer performances. A set of selected experimental data illustrates the isolated and interdependent influences of jet Reynolds number (Re), Taylor number (Ta) and rotating Grashof number (Gr_ω) on local and area-averaged Nusselt numbers (Nu and $\overline{Nu}$). With the present parametric conditions examined, the coupled Re, Ta and Gr_ω effects have led the ratios of rotational and non-rotational $\overline{Nu}$ in the range of 0.75–1.48. In conformity with the experimentally revealed heat transfer physics, the heat transfer correlation that permits the evaluation of $\overline{Nu}$ over the outer cylinder of the concentric annulus subject to jet-array impingement from the rotating inner cylinder is generated.

1. Introduction

Pressure driven Poiseuille flows in an annulus between a rotating inner cylinder and a static outer cylinder find a variety of engineering applications. The cooling of rotating electrical machineries by way of a rotor-mounted fan is but an example that feeds coolant into the annulus of small gap by imposing axial pressure gradients. Although it is inefficient to feed the coolant flow into the annulus between rotor and stator windings using a cooling fan attached on the rotor, this cooling measure is convenient and widespread for rotor machines with small powers. But with high power electric rotor machines, complex and external cooling schemes have to be employed in order to remove the large amount of heating power. As an attempt to efficiently feed the air coolant into the annulus between rotor and stator windings, which simultaneously offers high heat transfer rates and avoids the complexities of external cooling schemes adopted currently, this research group develops the impinging jet-array cooling system for electric rotor machines. The pressurized airflows are channeled through the hollow shaft of the rotor from the rotary seal toward the nozzles allocated on the outer surface of the rotating armature. Coolant jets impinge onto the stators with spent flows directed toward two annular exits at both ends of this rotor machine. This manner of coolant transportation is more effective than the rotor-fan assembly in view of cooling for the rotor and stator of rotating machinery. No previous study investigated the flow system; but a large amount of relevant works studied the flow and heat transfer phenomena for annular flows with a rotating inner cylinder [1–13] and the impinging jets [14–33].

The instability of a viscous fluid containing between two concentric rotating cylinders gives rise to Taylor vortices [1] which are characterized by trains of cellular vortices along the annulus. Such instabilities are triggered by the adverse gradient of angular momentum that competes with the viscous forces. When the centrifugal-force overcomes the stabilizing viscous flow, these two opposing forces create instability that produces a series of counter rotating vortices. As the centrifugal-force increases, this flow system undergoes a bifurcation sequence of dynamical transitions as reported by Kataoka [2]. For wavy Taylor vortex flow, the fluid mixes within each vortex as well as across cell boundaries via intercellular mixings that induce axial transport of fluids between vortices [3,4]. The wavy Taylor vortices, which are characterized by azimuthal traveling waves undulating in the axial direction; evolve into more complex patterns due to the appearance of turbulent patches as the rotation rate is further increased; and become the fully turbulent Taylor vortex flow eventually. With present applications that introduce axial/radial temperature gradients as well

* Corresponding author.
E-mail address: swchang@mail.nkmu.edu.tw (S.W. Chang).

0017-9310/$ - see front matter © 2008 Elsevier Ltd. All rights reserved.
doi:10.1016/j.ijheatmasstransfer.2008.08.023

Nomenclature

A,B,C_s,D_s	functional coefficients
d_j	jet diameter (m)
g	gravitational acceleration (ms^{-2})
Gr_g	gravitational Grashof number = $g\beta(T_w - T_b)d_j^3/\upsilon^2$
Gr_ω	rotating Grashof number = $\omega^2(D_i/2)\beta(T_w - T_b)d_j^3/\upsilon^2$
k_f	thermal conductivity of coolant ($Wm^{-1}K^{-1}$)
L	length of outer cylinder (m)
Nu	Nusselt number = $q_f d/(T_w - T_j)k_f$
$\overline{Nu}$	area-averaged Nusselt number
Pr	Prandtl number = $\mu C_p/k_f$
q_f	local heat flux (Wm^{-2})
Re	Reynolds number based on jet diameter = $V_j D_j/\upsilon$
Re_a	Reynolds number based on hydraulic diameter of annulus = $V_a(D_o - D_i)/\upsilon$
R_i	Radius of inner cylinder (m)
R_o	Radius of outer cylinder (m)
Ta	Taylor number = $4\omega^2 R_i^2(R_o - R_i)^3/[\upsilon^2(R_o + R_i)]$
T_b	local fluid bulk temperature (K)
T_j	jet temperature (K)
T_w	wall temperature (K)
V_a	mean axial velocity in annulus (ms^{-1})
V_j	jet velocity at nozzle exit (ms^{-1})
X	axial coordinate (m)

Greek symbols

Ψ	Unknown function
β	thermal expansion coefficient of coolant (K^{-1})
θ	angular coordinate (degree)
υ	kinematic viscosity of coolant (m^2s^{-1})
ω	angular velocity of rotating inter cylinder ($rads^{-1}$)

Subscript

0	steady-jet condition

as axial flows to Taylor–Couette flows, the convective mechanisms are further complicated. With radial temperature gradients across Taylor–Couette flow, the stability boundary of Taylor–Couette flow was influenced by the ratio of centrifugal and gravitational potentials as well as the Prandtl (Pr) and Grashof (Gr) numbers [5]. When the ratios of centrifugal to gravitational accelerations (γ) become relatively large, the density variations in Taylor–Couette flow are important for instabilities which are primarily centrifugal. The higher mode spirals were formed and the sinusoidal Nu variations over the surfaces of inner and outer cylinders were reported for a certain Gr range [6]. Heat transfer performances were generally improved as the rotation rates of inner cylinder increased [6]. In a recent numerical study [7], the area-averaged Nu in a horizontal annulus with hot rotating inner cylinder was found to increase with the increase of the buoyancy level.

The superposition of axial flow on Taylor–Couette flow induced several different spatiotemporal stable states and tended to stabilize the flow by delaying the formation of vortices up to higher rotations and inhibit some bifurcations that were present in the closed Taylor–Couette flows [8,9]. Depending upon Taylor (Ta) and axial Reynolds (Re_a) numbers, a rich mode of flow regimes occur with the geometry and transport properties of Taylor vortices disrupted. At low Re_a, Taylor vortices were winded by the axial flow and traveled in the direction of axial flow [10]. But at the higher Re_a, the convective motion of axial flow becomes less marked with a strong coupling between the imposed axial flow and the rotational flow. With flows at high Re_a, Taylor vortices are broken into spirals that disrupt the symmetry of Taylor–Couette flow by deforming and overlapping these vortices [11]. While for a turbulent Taylor–Couette–Poiseuille flow, the rotation on inner cylinder exhibits vague impacts on the axial turbulent intensity but provides significant changes on the radial and azimuthal turbulence intensities; which influences are enhanced as the rotation rate of inner cylinder increases [12]. With the test conditions of $500 \leqslant Re_a \leqslant 2800$ and $3 \times 10^3 \leqslant Ta \leqslant 8 \times 10^6$, three flow regimes that exhibited different heat transfer characteristics were resolved by increasing Ta systematically, namely a laminar flow regime giving an almost uniform $Nu \rightarrow$ a transition to vortex flow regime giving a sharp Nu increase $\rightarrow$ a third regime occurring at $Ta > 10^6$ where a reduction in Nu was observed [13]. The third flow regime where Nu decreases as Ta increases has not been previously reported before Wan and Coney [13] due to the relative low Ta examined by previous workers. Jeng et al. [14] attempted further heat transfer augmentations for the Taylor–Couette–Poiseuille flow by mounting the longitudinal ribs on the rotating inner cylinder. The typical flow and heat transfer performances for such enhanced Taylor–Couette–Poiseuille flow [14] were basically retained but the rib-induced flow features elevated the Nusselt numbers to the levels about 1.4 times of those acquired from the rotating inner cylinder with smooth wall.

In view of the cooling performances over the stagnation regions of jet array, the heat transfer studies for impinging jets are relevant but of different configuration. Depending on the distribution of jet nozzles [15,16], interactions of wall-jet [17–20], cross-flow [21–23], exit condition of spent flow [24,25], drainage [26,27], jet pulsation [28–30] and curvature of impinging surface [31–34], various heat transfer performances of impinging jets were reported. In addition to the aforementioned heat transfer physics in association with the impinging jets [1–27], the rotation of inner cylinder, through which the high momentum jets are issued toward the outer static wall, results in the jet intermittency on the impinging surface. Heat transfer studies of impinging jets involving flow pulsations [28–30] become relevant. Owing to the non-linear dynamic response of the hydraulic and thermal boundary layers to the pulsation of jets, the large coherent flow structures associated with the high-amplitude and high-frequency flow pulse in jet-stream increases stagnation Nu by surface renewal effect. At Strouhal numbers (St) lower than 0.05 and pulse amplitudes less than 17% of jet-flow, heat transfer levels were decreased from the steady-jet ones [29]. Such impairing heat transfer effect reflects that the disturbances associated with flow pulsation prohibit the momentum and energy transfer to equilibrate with the boundary-layers [29]. With jet intermittency, the similar heat transfer scenarios with those of pulsating jets were reported [30]. Depending on the frequency of jet intermittency, heat transfer levels in the stagnation region could be increased or decreased from the steady impinging jet levels, and the heat transfer generally increased with high-frequency of intermittency due to the boundary-layer renewal effect [30]. For occasions with curved impinging surfaces such as the present cooling applications for stator, the curved surfaces are known to elevate the overall heat transfer performances due to onset of secondary flows generated by the surface curvature [31–34]. Gau and Chung [31] observed Taylor-Görtler vortices initiated along a semi-cylindrical concave surface that enhance the momentum transport in the wall-jet region and improve heat transfer performances over the region near the stagnation point. While the area averaged heat transfer rates were increased, the stagnation Nu values on the concave impinging surface were almost as same

as those on flat surface [32–34]. Effects of surface curvature on heat transfer performances are enhanced as *Re* increases [32]. Neither the flow configurations nor the heat transfer characteristics of the rotating impinging jet-array onto the static cylindrical wall have been previously reported in the open literature. This cooling scheme mainly utilizes the high convective capability of impinging jet-arrays subject to intermittency due to rotation. But the flow structures in the jet-stream, stagnation and wall-jet regions are developed in the annulus with a rotating inner cylinder. Justified by the previous studies relevant to the flow system examined here [1–34], the heat transfer performances over the static outer cylinder are functionally related with Re_a, *Ta*, *Gr* and those controlling flow and geometric parameters for impinging jet-array.

2. Experimental details

2.1. Facilities

Fig. 1a and b, respectively, show (a) the rotating rig and (b) the heat transfer test module. As depicted in Fig. 1a, the rotating rig consists of a hollow shaft (1), the test platform (2) and three main bearings (3)-(5). The heat transfer test module (6) is supported between main bearings (3) and (5). Prior to entering the heat transfer test module (6), the test coolant (pressurized dry air) is fed from the rotary seal (7) into the heat transfer test module (6) and flows through the pressure regulator/filter (8) and the unit consisting of a needle valve (9), a flow meter (10), a thermometer (11) and a pressure transducer (12), within which the mass flow rate of coolant is adjusted and detected. The outer cylinder of the heat transfer test module (6) is made of a 0.1 mm thick stainless steel heating foil through which the electrical current is supplied to generate the uniform heat flux. The inner cylinder connected between two main bearings (3) and (5) is driven by an electrical DC motor (13) with adjustable speeds. The speed of rotation is detected by the optical detector (14) that converts the speed signal into the frequency signal. The electrical heater power is adjusted and metered by the heating power regulating unit (15). Thirty six thermocouples (16) with regular intervals are aligned along the outer cylinder (heating foil) to measure the axial (*X* wise) wall temperature distributions. These thermocouple signals are monitored by a PC via the Net-Daq Fluke Hydra 2645A data logger (17). A set of silver–silver instrumentation slip ring unit (18) is attached at the opposite end of the rotor seal (7) to transmit the thermocouple signals for jet temperatures to the data logger (17). The airflow for heat transfer tests is dehumidified and cooled to the ambient temperature through a refrigerating unit that is integrated with an air tank (19) fed by the screw-type compressor unit (20).

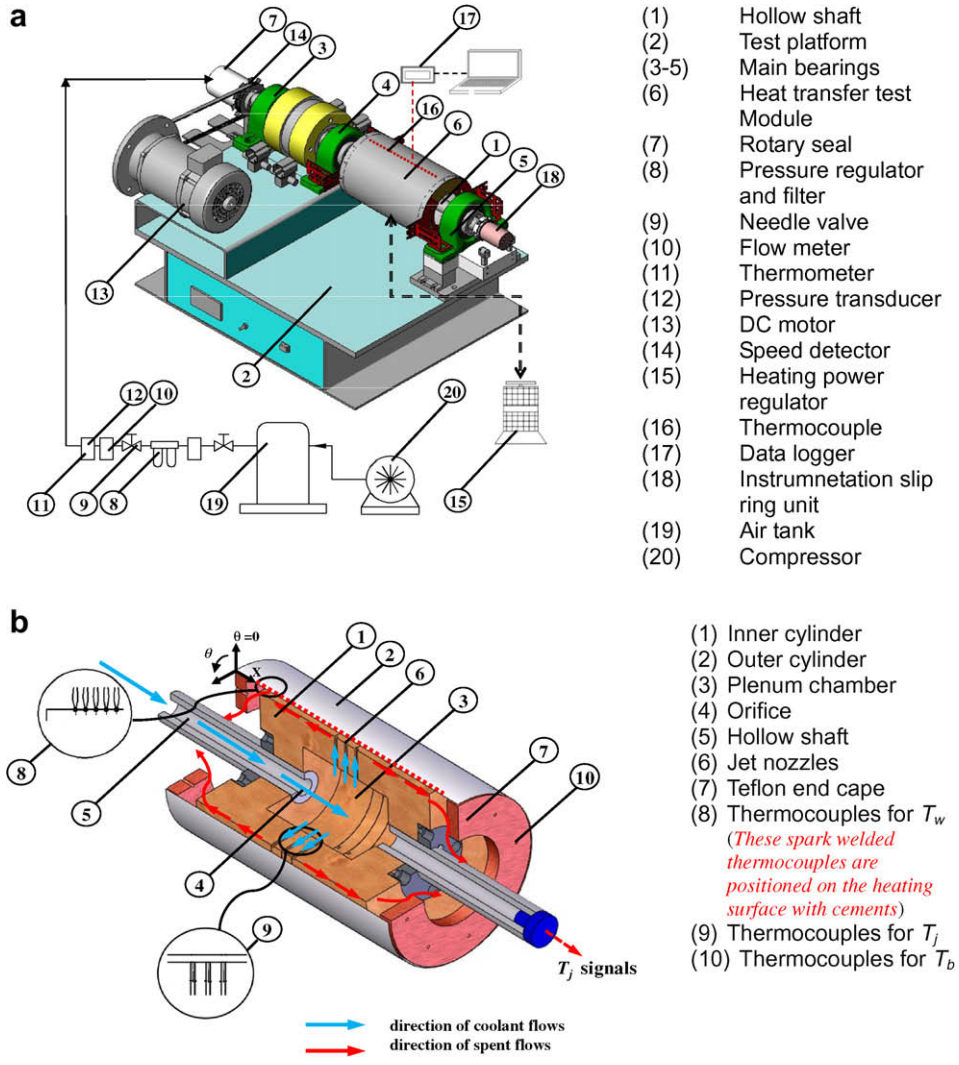

Fig. 1. Experimental test facility (a) rotating rig (b) heat transfer module.

Fig. 1b shows the sectioned view of the heat transfer test module which consists of the inner (1) and outer (2) cylinders. The inner and outer cylinders share the same length (L) of 260 mm with diameters of 148 and 160 mm respectively. The origin of coordinate system adopted by this study is positioned on the axial edge of the outer cylinder (2) as indicated in Fig. 1b. The test coolant vents into the plenum chamber (3) of 80 mm in diameter via four 5 mm orifices (4) through the hollow shaft (5). Four rows of circular nozzles in the diameter (D_j) of 3 mm (6) are arranged of an equal angular interval of 90°. Each jet-row consists of three jets with the pitch of 12 mm ($4D_j$) between two adjacent nozzles. The center of the central nozzle in each jet-row corresponds precisely to the axial location of $X = L/2$. The 4×3 nozzle-array impinges air-jets onto the outer cylinder (2) which is made of 0.1 mm stainless steel foil. Two streams of spent-fluid flow axially within the annular passage between the inner and outer cylinders from the central region toward two flow exits at two end caps made of Teflon (7). The annular area for venting the spent flow from each exit (7) is 3710 mm^2. Thirty six thermocouples (8) with the equal interval of 6.5 mm are attached on the outer cylinder (2) to detect the axial distributions of wall temperature (T_w). Three additional thermocouples (9) measure the jet temperatures (T_j) are guided through the hollow shaft to connect with the instrumentation slip ring for T_j measurements. Through the end cap (7), six thermocouples (10) along the central circumference with the angular interval of 60° penetrate into the core of exit flow passage to measure the fluid bulk temperatures (T_b). Fiber glass thermal insulation layers are wrapped around the outer cylinder in order to minimize the external heat loss.

2.2. Program and procedures

This study adopts the parametric approach to characterize the heat transfer performances of the impinging jet-array issued from the rotating inner cylinder in the Taylor–Couette–Poiseuille annular flow using the controlling dimensionless flow parameters for a set of predefined geometric conditions specified in Fig. 1b. This parametric analysis is devised to disclose the functional relationship of:

$$Nu = \Psi\{Re(Re_a), Ta, Gr_g, Gr_\omega, X, \theta\} \quad (1)$$

in which Ta (Taylor number) is the ratio between the rotating and viscous force effects and also indexes the intermittency frequencies of jets and spent flows. With the jets issued from the rotating inner cylinder, buoyancy interactions are further complicated from the Gr_g specified steady-jet conditions to the centrifugal-force manifesting Gr_ω impacts. It is noticed that, Eq. (1) derived for this study is specific to the particular configuration as depicted in Fig. 1b and therefore with limited use. However, the heat transfer characteristics as well as the methodology devised to generate the design correlation are applicable for this type of flow configuration. Variations in local and area-averaged Nusselt numbers caused by the individual and interactive effects of the controlling dimensionless parameters in Eq. (1) are examined with the heat transfer correlations for area-averaged Nusselt numbers derived. By way of setting the controlling flow parameters in Eq. (1), the flow field in the concentric annulus is accordingly generated and the influences of varying $Re(Re_a)$, Ta, Gr_g and Gr_ω on heat transfer rates over the impinging outer cylinder are systematically examined. The tested jet Reynolds numbers (Re) in the range of 10000-40000 ensure the turbulent jets while the annular flow Reynolds numbers specified by the hydraulic diameter of the concentric annulus (Re_a) in the range of 600-2400 characterized the laminar flow. Turbulence activities in association with the turbulent jets are interacting with the laminar Taylor–Couette–Poiseuille annular flow where the viscous effects are likely to damp out the turbulent fluctuations when the spent-fluids convect for the stagnation region toward two end exits. The ranges of the non-dimensional parameters investigated by the present study are summarized in Table 1.

Table 1
Ranges of experimental parameters investigated

Jet Reynolds number (Re)	10000, 20000, 30000, 40000
Annular flow Reynolds number (Re_a)	600, 1200, 1800, 2400
Taylor number (Ta)	400000–15000000
Gravitational Gashof number (Gr_g)	0–400
Rotating Gashof number (Gr_ω)	0–130000

This experimental study involves three phases. The first phase examines the effects of $Re(Re_a)$ and Gr_g on local (Nu_0) and area averaged ($\overline{Nu}_0$) Nusselt numbers by performing a series of baseline heat transfer tests with the inner cylinder remaining static at $Re(Re_a)$ = 10000(600), 20000(1200), 30000(1800) and 40000 (2400). At each selected $Re(Re_a)$, heat transfer tests are conducted with five ascending heat fluxes to generate five sets of Nu_0 data corresponding to different Gr_g. For each set of $Re(Re_a)$ and heat flux, the axial heat transfer distributions constituted by 36 local Nu_0 data along the outer cylinder are detected at 36 angular locations with 5° intervals from 0° to 180°. Measurements of axial Nu_0 distribution at predefined angular locations are performed by adjusting the angular location of the outer heating foil in respect to the axis of $\theta = 0°$ as indicated in Fig. 1b.

The second phase of program performs the heat transfer tests with the rotating inner cylinder at speeds of 500, 1000, 1500 and 2000 rev/min. The axial thermocouples are aligned with the angular location of $\theta = 0°$ for all the rotating tests. The $Re(Re_a)$ and heating powers selected for non-rotational tests are repeated at each tested rotating speed. Heat transfer results from the first and second phases are compared to reveal the heat transfer modifications caused by the rotating flow parameters, namely the Taylor (Ta) and rotational Grashof (Gr_ω) numbers. The third phase of this program derives the heat transfer correlations to evaluate the area-averaged Nusselt number over the outer cylinder with the inner cylinder at both static and rotating conditions.

The heat transfer data is collected at the steady state which is assumed when the differences between the wall temperatures (T_w) on the impinging surface from several successive scans are less than 0.3 °C for each test condition. It generally takes about 45 min to reach the steady state when the variation of flow rate, heating power or rotational speed is made. Having satisfied the steady state condition, the on-line data acquisition system is activated to store the detected wall and fluid temperatures with all the relevant measurements such as the heating power and the flow rate to be recorded.

For the present impinging jets, the temperature differences between the adiabatic and jet temperatures are predefined less than 0.28 °C within the present range of $Re(Re_a)$. Therefore the reference fluid temperature for defining the local Nusselt number is replaced by the jet temperature (T_j) which is measured by the thermocouples in the flow passages connecting the jet-nozzles as indicated in Fig. 1. A silver–silver instrumentation slip ring unit transmits these thermocouple signals to the data logger that is linked with a PC for data monitoring and storage. The jet temperature (T_j) is evaluated as the averaged value from these thermocouple measurements. Along with the measured heating power, T_w and T_j, the local Nusselt number is evaluated as $Nu = (q_f D_j)/[k_f(T_w - T_j)]$ in which the convective heat flux (q_f) is calculated by subtracting the flux of heat loss from the total heat flux supplied. The total heat flux is obtained by dividing the heating power with the effective cooling area from the outer cylinder. The heat loss flux is proportional to the steady wall-to-ambient temperature difference. The proportionality between the heat loss flux and the wall-to-ambient

temperature difference for the present heat transfer module is determined through a series of heat loss calibration runs. This proportionality is incorporated into the data processing program to determine the local heat loss flux. However, with either steady or rotating impingement jet-array onto the outer cylinder of the annular flow, the distributions of T_w over the impinging surface are non-uniform. Consequently, the distribution of heat loss flux over the heating foil (outer cylinder) is accordingly non-uniform. As the heat loss coefficient is small due to the appropriate thermal insulation, the maximum heat loss is about 3.8% of the total heat flux. The maximum non-uniformity of convective heat flux over the outer cylinder is about 3.9%. The thermal conditions over the impinging outer cylinder are confirmed with the basically uniform heat fluxes.

Another worth noting effect on the quality of experimental data is the influences of fluid property variations on the dimensionless parameters evaluated. As the axial fluid temperature distributions from the stagnation region toward two end-exits approximately follow the trend of linear increase due to the uniform heating condition, the effect of variable fluid-properties due to temperature variations is accounted in according to the local fluid bulk temperature (T_b) defined by the enthalpy balance method. At each flow exit, five thermocouples penetrate into the core of the annular exit to measure the exit fluid temperatures. The fluid exit bulk temperature is the average of these thermocouple measurements, which is constantly checked with the calculated exit T_b to check for the accuracies of energy accountancy and flow-rate measurement. Data batches are accepted when the differences between the calculated and measured T_b at the flow exits are less than ±10%.

Experimental uncertainties of the controlling flow parameters and *Nu* are majorly attributed from the temperature measurements due to the variations of fluid-properties caused by T_b variations. The maximum uncertainty of the thermocouple readings is 0.3 °C. Following the policy of ASME on reporting the uncertainties in experimental measurements and results [35] with the heating powers in the range of 350–560 W and the wall-to-jet temperature differences of 45–120 °C, the maximum uncertainty associated with *Nu*, *Re*, *Ta*, Gr_g or Gr_ω are estimated as 9.8, 6.3, 4.6, 8.1 and 8.9% respectively.

3. Results and discussion

3.1. Impinging jet-array heat transfer in annulus with static inner cylinder

With the characteristic length defined as the jet diameter (d_j) of 3 mm by the present study, the conversions from *Re*, *Nu* based on D_j to the axial Reynolds (Re_a) and Nusselt (Nu_a) numbers based on the customary length scale for annular flows of $D_o - D_i$ (12 mm) follow the relationships of $Re_a = 0.06\,Re$ and $Nu_a = 4\,Nu$. Such conversions between *Re* versus Re_a and *Nu* versus Nu_a are followed by all the test results obtained with the static or rotating inner cylinder. In this section, the Nu_0 data collected from the outer cylinder with the stationary inner cylinder are examined to feature the heat transfer performances at the limiting conditions of $Ta = 0$.

The axial heat transfer distributions consists of 36 local Nu_0 data along the outer cylinder were measure 36 angular locations with 5° intervals from 0° to 180°. Fig. 2 depicts the Nu_0 distributions on the outer cylinder with four ascending buoyancy levels of (a) $Gr_g = 216$, (b) $Gr_g = 271$ (c) $Gr_g = 329$ (d) $Gr_g = 354$ at *Re* (Re_a) = 10000 (600). With all Gr_g and *Re* tested, the axisymmetric Nu_0 distributions over the outer cylinder are also axially symmetric about the midspan axis of $X/L = 0.5$ as exemplified by Fig. 2. Effects of jet-to-jet collisions in angular direction on Nu_0 distributions are clearly visible as the midway low Nu_0 regions between two adjacent jet-rows. With this flow configuration, three jets align with the axis of inner and outer cylinders to form a jet-row. There are four jet-rows with equal intervals of 90° that issue high momentum jets toward the outer cylinder. Jet-to-jet interactions in the axial and angular directions respectively take place within each jet-row and between two adjacent jet-rows with 90° intervals. The heated spent-fluid flows after impingements are initially developed within the narrow annulus of height = $2D_j$ in both axial and angular directions. But due to the lack of vents for angular spent-fluid flows, all the heated spent-fluid flows are directed in the axial direction toward the two annular exits at $X/L = 0$ and 1. Along with the axial developments of wall-jet-flows, the outer wall temperatures increase axially from the stagnation region toward the two annular exits. The monotonic decays of Nu_0 from the high Nu_0 region, that is centered around the stagnation region, toward two exits are observed as shown in Fig. 2. But the collisions of angular spent-fluid flows from two adjacent jet-rows as well as the jet-to-jet interferences prior to and after the impingements considerably weaken and diffuse the momentum fluxes of these angular wall-jet-flows. As a result, the low Nu_0 regions showed by Fig. 2 constantly develop at the midways between two adjacent jet-rows along each circumference on the outer cylinder. The spent-fluids emanating from these midway regions between two adjacent jet-rows are diverted to the axial direction and heading toward the flow exits. When these heated streams emanating form the midways between two jet-rows convect axially in the annulus toward the exits, the momentum fluxes are further reduced by friction drags with the downstream boundary-layers thickened. Owing to the combined effects of the weakened flow momentum, the increased fluid temperatures and the thickened boundary-layers along the annulus, the worst heat transfer scenarios constantly develop at the axially downstream locations of the midways between two jet-rows as seen in Fig. 2. In particular, due to the different degrees of flow transitions, jet-to-jet interactions and spent-flow confinements in the angular and axial directions, the oval shaped stagnation heat transfer regions are observed in Fig. 2. At *Re* = 10,000, the oval stagnation Nu_0 region covers an angular span of about 40° and the axial span of 0.4 X/L as seen in each plot of Fig. 2. Each of these oval shaped stagnation Nu_0 regions shows a longer axial stretch than its angular span. This reflects the improved fluency for the spent-fluid flow in the axial direction than its angular counterpart due to the locations of flow exits. As the jet-streams issued from the four jet-arrays are confined in the annulus, intensive interactions between the heated spent-fluid flows and the jet-streams prior to and after the impingements are expected. Variations of flow structures as well as the density distributions of wall-jet-flows in the annulus can alter the transfer processes of momentum and heat by way of altering the jet-to-jet interferences and the interacting manners between the jet-streams and the surrounding spent-fluid flows. This flow physics can lead to buoyancy effects on the heat transfer process examined here when the distributions of fluid density in the annulus are varied by adjusting the heating level imposed on the outer cylinder. The sequential examination of Nu_0 distributions showed by Fig. 2a,b,c,d indicates the systematic variations of Nu_0 distributions driven by increasing Gr_g from 216 to 354. As Gr_g increases, the area-averaged Nu_0 over the outer cylinder ($\overline{Nu}_0$), as indicated in each plot of Fig. 2, decreases consistently with the spatial ranges of stagnation regions reduced. Another worth noting impacts on Nu_0 distributions caused by increasing Gr_g is the moderated spatial Nu_0 variations. Owing to the absence of Taylor–Couette flow instabilities as $Ta = 0$, the reduced $\overline{Nu}_0$ along with the diffused Nu_0 contours triggered by the systematic increase of Gr_g are mainly attributed to the entrainment of heated spent fluids into the cold jets issued from the inner cylinder. With the higher heat flux transferred into the annular wall-jet-flow, the entrainment of the hotter and less dense fluids into the cold free-jets warms up the jet-streams prior to impinge-

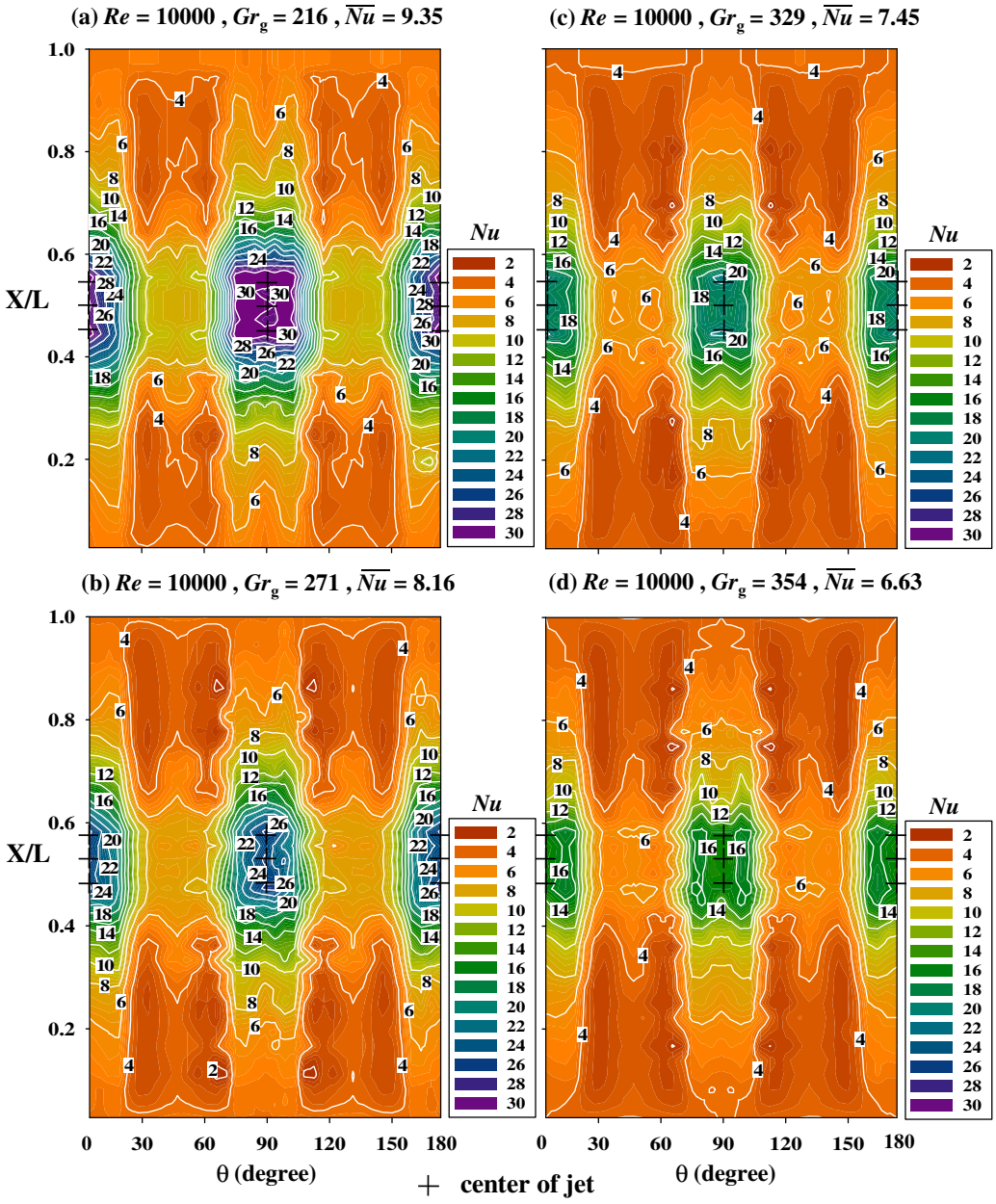

Fig. 2. Nu_o distributions over the outer cylinder at Re=10000 with (a) Gr_g = 216, (b) Gr_g = 271, (c) Gr_g = 329, (d) Gr_g = 354.

ments and also weakens the jet-momentum by diffusing the density of jet-stream. With the inner cylinder remaining stationary, the mechanics responsible for improving heat transfer performances by imposing the radial temperature gradients in the Taylor–Couette–Poiseuille flows in the horizontal annulus with rotating inner cylinder [7] are absent. Instead, the weakened jet momentums by diffusing the densities of jet-streams with the higher jet temperatures due to the severe jet entrainment in the narrow annulus impair the overall heat transfer performance in terms of $\overline{Nu}_0$.

A more clear vision of buoyancy effects on heat transfer performances over the outer cylinder is depicted in Fig. 3 where the axial Nu_0 profiles at the angular locations of (a) 0° (b) 15° (c) 30° (d) 45° (e) 60° (f) 75° with four ascending Gr_g levels at Re = 20000 (Re_a = 1200) are compared. The data points in each Nu_0 profile at the zero buoyancy condition (Gr_g = 0), as seen in each plot of Fig. 3, are inferred from the varying trend of Nu_0 against Gr_g at each measurement location. As shown in Fig. 3, the ranges of data spreads driven by varying Gr_g are X/L and θ dependent. The larger Gr_g-driven data-bands which reflect the higher degrees of buoyancy impacts on heat transfer are developed at the stagnation region. Away from the stagnation regions toward two exits at X/L = 0 and 1, the impacts of buoyancy effects featured by the Gr_g-driven data-bands are gradually faded as the flow structure yields from the impinging jets toward the annular flow. Each row of cold jets interacts with the hot annular spent-flows under a highly confined environment prior to impingements. As described previously, the entrainments of hot fluids into the cold jets impair the impinging heat transfer rates and diffuse the spatial Nu_0 variations. Such phenomenon is most evident at the stagnation points indicated in Fig. 3a. At the inferred zero-buoyancy condition, three Nu_0 values at three stagnation points of the jet-row are equivalent and clearly visible in Fig. 3a. But the systematic increase of Gr_g causes the stagnation Nu_0 at the central jet of this jet-row to reduce accord-

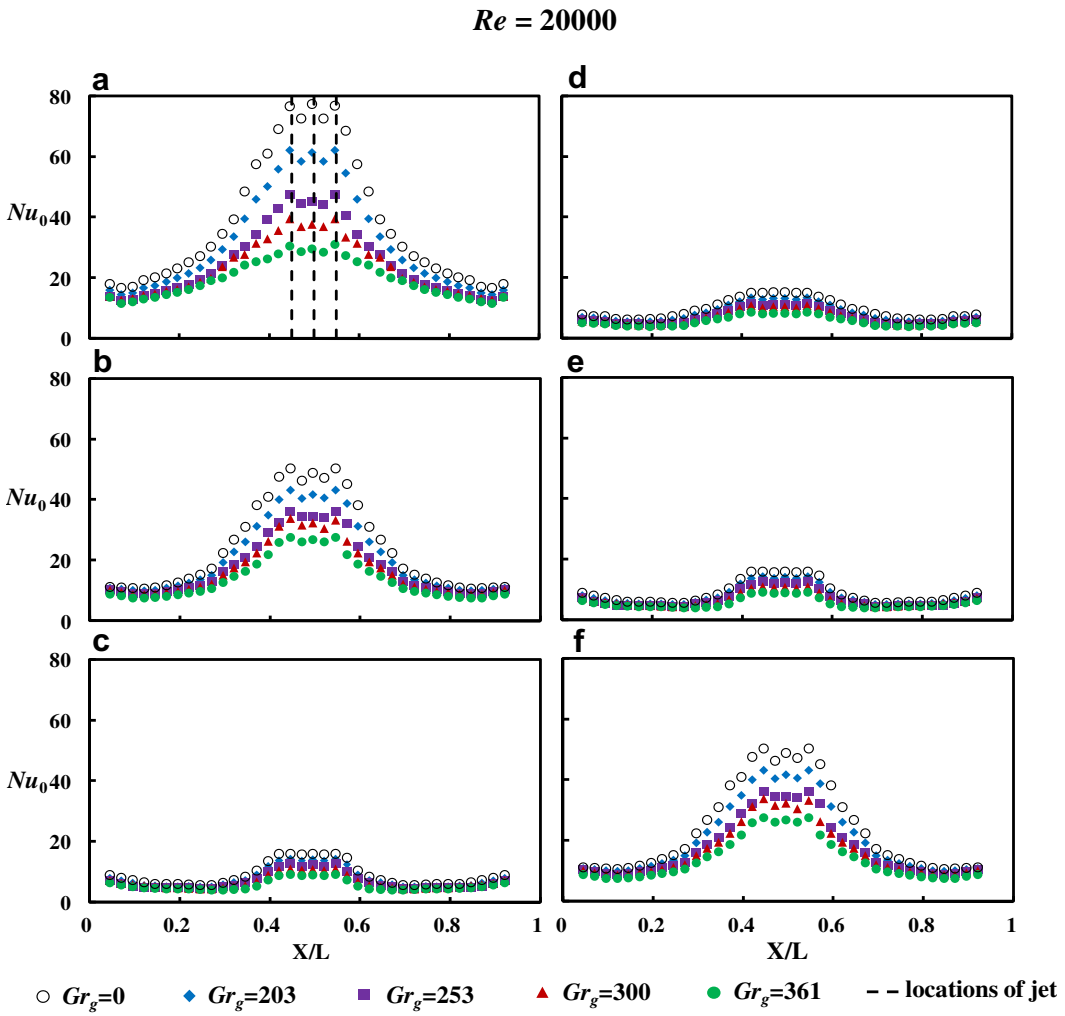

Fig. 3. Axial Nu_o distributions with five Gr_g at Re=20000 along (a) $\theta = 0°$, (b) $\theta = 15°$, (c) $\theta = 30°$, (d) $\theta = 45°$, (e) $\theta = 60°$, (f) $\theta = 75°$.

ingly as depicted in Fig. 3a. By elevating Gr_g systematically, the reduced stagnation Nu_0 of central jet in each jet-row along with the moderated spatial Nu_0 variations in the stagnation region demonstrate the enhanced effects of jet entrainments and jet-to-jet interferences prior to and after the impingements over the stagnation region. Angular variations of axial Nu_0 profiles and buoyancy impacts are revealed by way of examining the Nu_0 data collected in Fig. 3a,b,c,d,e,f. In view of such θ-wise variations in axial Nu_0 profiles, the typical Nu_0 distributions for impinging jet-array are featured in Fig. 3a,b and f. But at the midways between two impinging jet-rows ($\theta = 45°$), the collisions of spent-fluid flows in the angular direction produce the lowest Nu_0 levels as well as the least Gr_g-driven data-bands at the stagnation regions. In the angular locations of $30° \leqslant \theta \leqslant 60°$ showed by Fig. 3c,d and e, the Gr_g-driven data bands are considerably reduced from the angular locations nearby the stagnation points (see Fig. 3a,b and f) where the jet entrainments are providing a considerable impact on heat transfer process. Clearly, the effects of entraining hot spent-fluids into the cold jets which produce the attendant buoyancy effects are systematically faded in the angular direction as fluids move away from the stagnation point ($\theta = 0°$) toward the midway between two adjacent jet-rows ($\theta = 0° \rightarrow 45°$ or $\theta = 90° \rightarrow 45°$).

Fig. 4 examines the variations of Nu_0 distribution as Re increases from (a) $Re(Re_a) = 10000(600) \rightarrow$ (b) $Re(Re_a) = 20000(1200) \rightarrow$ (c) $Re(Re_a) = 30000(1800) \rightarrow$ (d) $Re(Re_a) = 40000$ (2400) at a nominal buoyancy level of about $Gr_g = 300$. As shown in Fig. 4, increases of Re consistently elevate the area averaged $\overline{Nu}_0$ and elongate the axial span of stagnation region but can not cause a noticeable extension in angular span for the stagnation region. Unlike the buoyancy impacts revealed in Fig. 3 that are location (X/L and θ) dependent, the pattern of heat transfer distributions is followed by all the test results obtained with different Re as shown in Fig. 4. Flow structures developed in the concentric annulus with jets issuing from the static cylinder are not considerably modified as Re varies. Therefore the increase of Re incurs rather uniform Nu_0 elevations all over the outer cylinder. This is better illustrated by examining the variations of axial Nu_0 profiles driven by increasing $Re(Re_a)$ from 10000(600) to 40000(2400) at θ = (a) 0° (b) 15° (c) 30° (d) 45° (e) 60° (f) 75° with a fixed Gr_g as seen in Fig. 5. For ach plot collected in Fig. 5, the increase of Re elevates the entire set of axial Nu_0 profile. Although the characteristic Nu_0 distribution along the annulus at each θ location depicted by Fig. 5 follows the typically axial Nu_0 profile showed in Fig. 3, but the Nu_0 elevations owing to the increase of Re prevail over the entire axial span irrespective of the different flow structures between impinging-jet and annular flows at the central and end regions respectively.

Fig. 6a and b, respectively, depict the variations of $\overline{Nu}_0$ versus Gr_g at the fixed Re and versus Re at the fixed Gr_g. Followed by the heat transfer physics demonstrated in Figs. 2,3, $\overline{Nu}_0$ decreases linearly as Gr_g increases at each tested Re as shown in Fig. 6a. Although the slope for each data trend at a fixed Re showed by Fig. 6 a remains negative, the magnitude of slope for each Re controlled data trend in

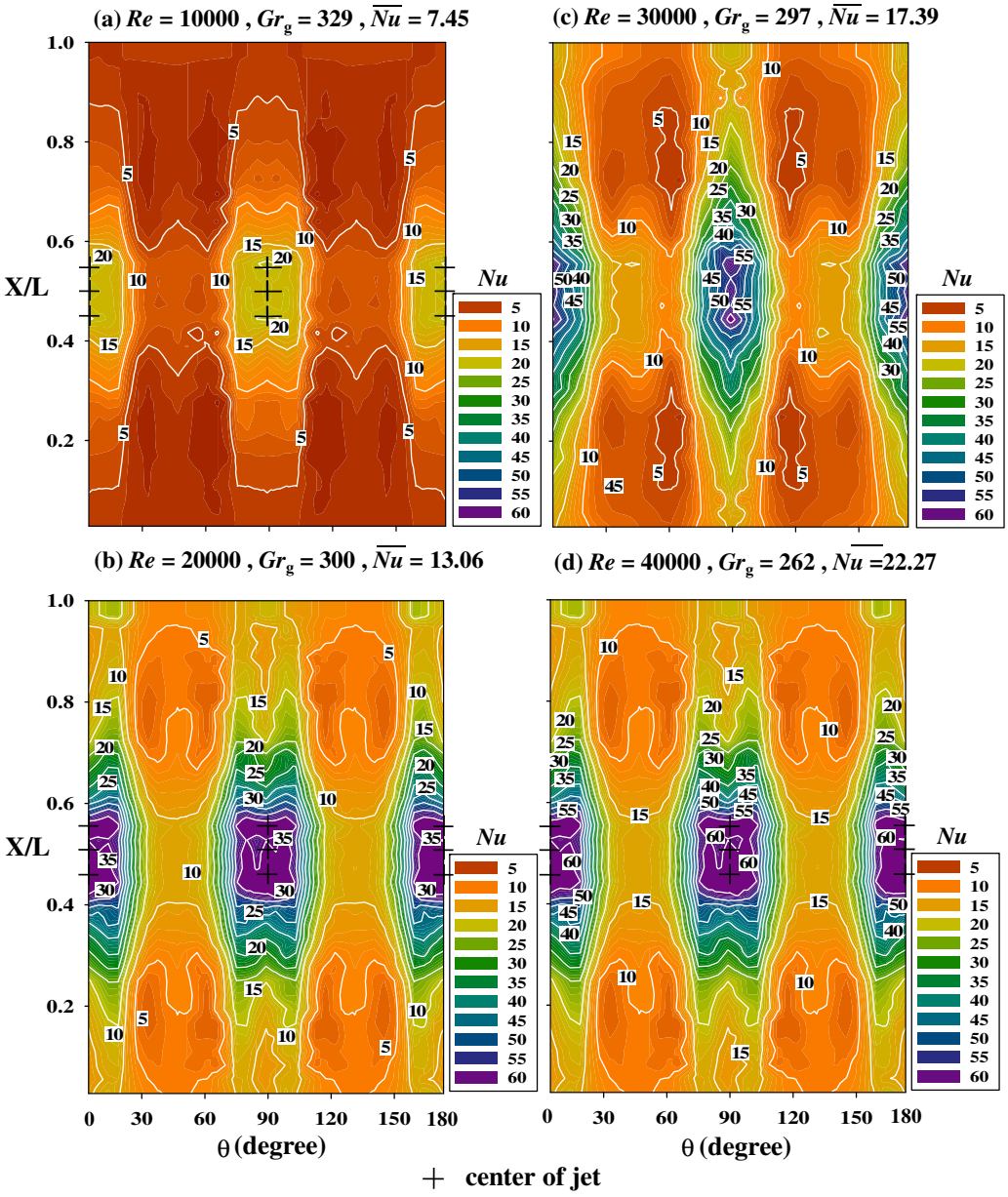

Fig. 4. Nu_o distributions over the outer cylinder at a nominal Gr_g value with (a) Re = 10000, (b) Re = 20000, (c) Re = 30000, (d) Re = 40000.

this figure increases with the increase of Re. Buoyancy impacts on $\overline{Nu}_0$ is amplified at the higher Re. The $\overline{Nu}_0$ level inferred from each data trend obtained at a fixed $Re(Re_a)$ of 10000(600), 20000(1200), 30000(1800) and 40000(2400) corresponding to the limiting condition of $Gr_g = 0$ is also marked at the vertical axis of Fig. 6a. The so-called zero buoyancy $\overline{Nu}_0$ levels are accordingly generated using such extrapolating process. These inferred $\overline{Nu}_0$ at $Gr_g = 0$ along with the experimental $\overline{Nu}_0$ data are plotted against Re in Fig. 6b. Clearly, the degrees of Re impact on $\overline{Nu}_0$, which are reflected by the slope of each Gr_g controlled data trend in Fig. 6b, reduce systematically as Gr_g increases. Justified by the data trends depicted in Fig. 6a with the interdependency of Re and Gr_g effects on $\overline{Nu}_0$, the empirical $\overline{Nu}_0$ correlation takes the form of

$$\overline{Nu}_0 = A\{Re\} + B\{Re\} \times Gr_g \quad (2)$$

in which the functional values A and B correspond respectively to the zero buoyancy $\overline{Nu}_0$ levels and the slope of each Re controlled data trend in Fig. 6a. Justify by the varying manners of A, B coefficients against Re, $\overline{Nu}_0$ correlation is accordingly generated as Eq. (3).

$$\overline{Nu}_0 = 0.0114 \times Re^{0.76} - (0.00601 + 1.223 \times 10^{-6} \times Re) \times Gr_g \quad (3)$$

Eq. (3) correlates all the $\overline{Nu}_0$ data within ±10% discrepancies from the experimental data. The Re exponent of 0.76 in Eq. (3) is less than 0.8 which value is generally reported by many Nu_0 correlations derived for forced heat convection in channels such as the Dittus–Boelter correlation. The reduced Re exponent in Eq. (3) from 0.8 is owing to the presence of jet impingements in the annular flow. Eq. (3) is used to evaluate $\overline{Nu}_0$ over the outer cylinder with the inner cylinder remains stationary against which the Nu data collected from the outer cylinder with the rotating inner cylinder are compared.

3.2. Impinging jet-array heat transfer in annulus with rotating inner cylinder

Unlike the static results which show the θ-wise heat transfer variations in association with the locations of jets and Gr_g effects, the impinging jet-array issued from the rotating cylinder at the

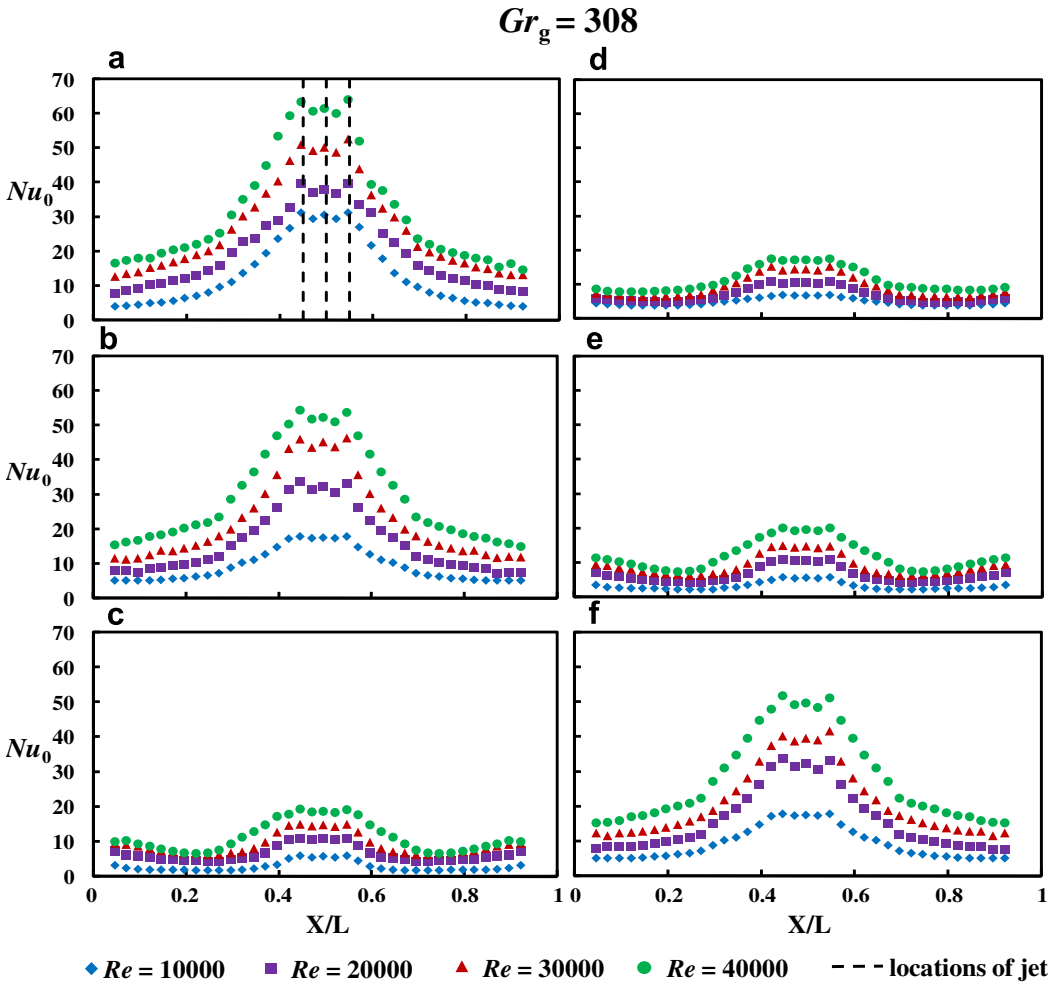

Fig. 5. Axial Nu_o distributions with four Re at $Gr_g = 308$ along (a) $\theta = 0°$, (b) $\theta = 15°$, (c) $\theta = 30°$, (d) $\theta = 45°$, (e) $\theta = 60°$, (f) $\theta = 75°$.

high speeds of 500–2000 rev/min breaks the flow physics responsible for θ-wise Nu_0 variations. But the flow and heat transfer of the impinging jet-array from the rotating inner cylinder with spent flows through the annulus are further complicated by the intermittencies of jets and spent flows over the outer cylinder. Frequencies of intermittency for present rotating jets fall in the range of 33.2–133.2 Hz and are proportional to Ta. With the rotating inner cylinder, the buoyancy effects on flow and heat transfer under the rotating environments are shifted from a stable mode characterized by Gr_g to a dynamic mode characterized by Gr_ω. The potential that drives buoyancy effects in the annulus with rotating inner cylinder is added by the centrifugal accelerations due to the rotation of the inner cylinder. Buoyancy interactions take place in a virtually unsteady flow field when the jet-array is issued from the rotating inner cylinder. However, due to the high frequencies of flow intermittency for present rotating conditions at all the test speeds, there are no appreciable θ-wise Nu variations. The rotational Nu values are spatial functions of X which are interdependent with $Re(Re_a)$, Ta and Gr_ω.

Fig. 7 depicts a set of X-wise Nu variations obtained at four different Gr_ω with fixed Ta at $Re(Re_a) = 20000(1200)$ in order to highlight the rotating buoyancy effect on local Nu. The Nu levels corresponding to the zero buoyancy condition ($Gr_\omega = 0$) as shown in Fig. 7 are obtained by the similar data extrapolating procedure demonstrated in Fig. 6a. As shown in each plot of Fig. 7, local Nu consistently increases as Gr_ω increases. Patterns of X-wise Nu distribution showed in Fig. 7 generally follow the results found for the static annulus with steady-jets. But the zigzag Nu_0 profiles in the stagnation region at the static test conditions are replaced by the rather uniform Nu distributions when the inner cylinder rotates. With impinging jets issuing from the rotating inner cylinder, the buoyancy effect improves heat transfer, which reverses the Gr_g effects that impair heat transfer in the static annulus. Locations where the Gr_ω effects are most evident as shown in Fig. 7 still develop in the stagnation region. When the coolant flows axially from the stagnation region toward two exits, the flow structures gradually yield from the rotating jet-array impingement toward the Taylor–Couette–Poiseuille flow. The spans of Nu data-bands driven by increasing Gr_ω in each plot of Fig. 7 are correspondingly reduced, indicating the axially weakened rotating buoyancy effects on heat transfer. With the rotating inner cylinder, the mechanics responsible for improving heat transfer by imposing radial temperature gradients in Taylor–Couette–Poiseuille flows within the horizontal annulus [7] can develop to improve heat transfer performances due to buoyancy effects. In particular, over the stagnation flow region where the rotating jets impinge on the outer cylinder, the intermittencies of jets and spent flows prohibit the stable entrainment of hot fluid into the rotating jets and consequently prevent the mechanics responsible for impairing static heat transfer by increasing buoyancy level. Augmentations of turbulence intensity [7] and/or vorticity as the combined effects of increasing the radial fluid temperature gradients with the presence

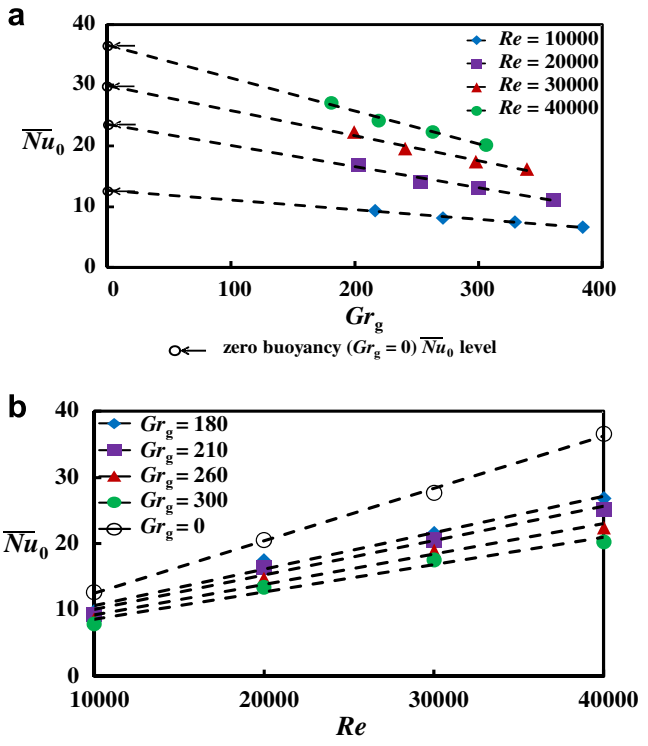

Fig. 6. Variations of $\overline{Nu}_0$ against (a) Gr_g at different Re and against (b) Re at different Gr_g.

of Taylor–Couette flow instabilities can still persist in the stagnation region and lead to heat transfer improvements by increasing Gr_ω in the stagnation region as seen in Fig. 7.

Another interesting rotational heat transfer result that is different from the static results showed by Figs. 3 and 5a is the rather uniform Nu distributions in the stagnation region as depicted in each plot of Fig. 7. Previous studies for pulsating jets involving jet intermittencies [28–30] observed the formation of coherent vortical jet-flow structures due to dynamic responses of hydraulic and thermal boundary-layers to the pulsation of jets. When jet pulsations are induced at low frequencies with small amplitudes, the impinging-jet heat transfer rates were decreased from the steady-jet ones [29]. But the heat transfer performances can be improved from the steady-jet levels with high-frequency of intermittency due to the boundary-layer renewal effect [30]. Even with the steady-jet impinging onto the concave curved wall, the presence of three semi-stable flow regimes in the vicinity of the concave surface involves flow oscillations [36]. These oscillatory impinging jet-flows can induce the flow recirculation which elevates the fluid temperatures adjoining the heated concave wall. Using the jet temperature as the referenced fluid temperature to determine Nu, the increased wall temperatures near the stagnation points suppress the maximum heat transfer peaks at the stagnation points and lead to the more uniform Nu distribution over the stagnation region. Another flow physics in association with the more uniform Nu profiles over the stagnation region as seen in Fig. 7 is the modified jet-to-jet interactions from the static scenarios when the impinging jets rotate. With the static inner cylinder, the thickened boundary-layers constantly develop at the midways between two adjacent jets where the relatively low Nu_0 are observed as a result of jet-to-jet collisions. Nevertheless, the rotation of jet-array causes the impinging jets to periodically "wash" the outer cylinder and breaks the thickened boundary-layers at midways between two adjacent jets. Such intermittent washing effect is driven by rotating the jets and prohibits the development of stable thickened boundary layers due to jet-to-jet collisions. Consequently, the impairing heat transfer effects at the midways between two adjacent jets are weakened. Depending on Ta at each specified $Re(Re_a)$, the rotational Nu levels can be increased or decreased from the static Nu_0 levels due to the intermittencies of jets and spent flows. The opposing buoyancy effects which respectively improve and impair heat

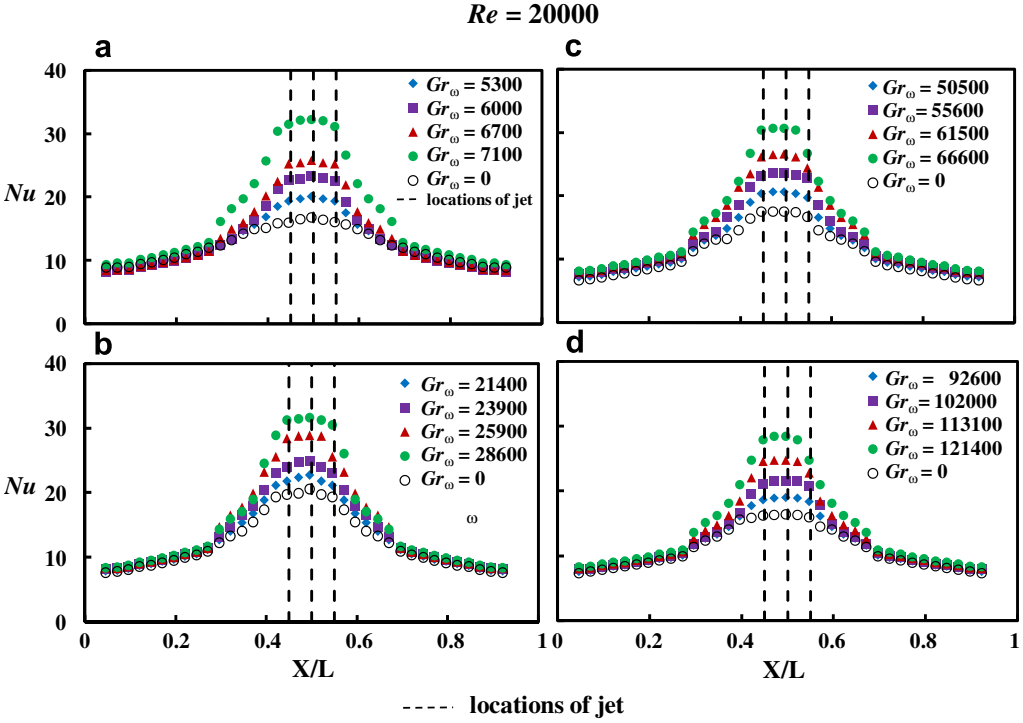

Fig. 7. Axial Nu distributions with five Gr_ω at Re = 20000 with (a) Ta = 603000, (b) Ta = 2432000, (c) Ta = 5519000, (d) Ta = 9899000.

transfer performances with rotating and steady-jets can assist to improve the cooling performances of the present rotating impinging jet-array from the static condition.

Each plot in Fig. 8 compares five sets of X-wise Nu distribution detected form different Ta with the fixed $Re(Re_a)$ and $\beta(T_w - T_j)$. Due to the combined Ta, $Re(Re_a)$ and Gr_ω effects, the Nu values obtained from the rotating tests are increased or decreased from the static Nu_0 references ($Ta = 0$) as compared in Fig. 8. For all the rotating conditions examined here, the increase of Ta generally reduces Nu at each X location. The relatively large Nu spreads driven by varying Ta develop in the stagnation region where the jet-washing effect and the intermittencies of jets and spent flows are most evident. Similar to the axial decay of Gr_ω impacts as depicted in Fig. 7, such Ta driven Nu spreads are continuously reduced when the coolant flows axially toward two exits. This reflects the axially weakened Ta impacts as the flow transits from the stagnation wall-jet-flow to the Taylor–Couette–Poiseuille flow. However, as the increase of Ta incurs a systematic reduction in Nu at each X location, the parametric conditions in terms of Ta and $Re(Re_a)$ examined here are likely to fall in the range where the intermittencies of jets and spent flows impede local heat transfer rates from the steady-jet ones. To confirm this particular heat transfer result, the isolated Ta impacts on Nu need to be identified.

In the attempt to determine the isolated Ta impacts on heat transfer, the procedure devised to identify the heat transfer levels at the zero-buoyancy conditions as demonstrated in Fig. 6a is repeated to analyze the rotational heat transfer data. In order to highlight the heat transfer modifications from the static references, the rotational heat transfer results are presented in terms of $\overline{Nu}/\overline{Nu}_0$ in which $\overline{Nu}$ quotes the X-wise averaged Nu obtained at the predefined $Re(Re_a)$, Ta and Gr_ω. The data trends of $\overline{Nu}/\overline{Nu}_0$ versus Gr_ω at the selected $Re(Re_a)$ and Ta are displayed in Fig. 9. At any fixed $Re(Re_a)$ and Ta, each set of $\overline{Nu}/\overline{Nu}_0$ shown in Fig. 9 increases linearly as Gr_ω increases. The $\overline{Nu}/\overline{Nu}_0$ correlation is accordingly defined by Eq. (4) where C and D coefficients are functions of Re and Ta.

$$\overline{Nu}/\overline{Nu}_0 = C\{Re, Ta\} + D\{Re, Ta\} \times Gr_\omega \tag{4}$$

The so called zero-buoyancy $\overline{Nu}/\overline{Nu}_0$ (C values) which are marked on the vertical axis of each plot in Fig. 9 are identified by extrapolating these Gr_ω controlled data trends to the limiting conditions of $Gr_\omega \to 0$. Clearly, these zero-buoyancy $\overline{Nu}/\overline{Nu}_0$ data are Ta and $Re(Re_a)$ dependent. Coefficients C in Eq. (4) physically represent the $\overline{Nu}/\overline{Nu}_0$ levels at the zero-buoyancy conditions while Re and Ta remain finite. As D coefficients within the parametric range tested are positive, heat transfer improvements due to the rotating buoyancy effect are reconfirmed. The varying manners of $\overline{Nu}/\overline{Nu}_0$ obtained with vanished buoyancy effect against Ta at the fixed $Re(Re_a)$ are collected in Fig. 10. As shown in Fig. 10, each set of zero-buoyancy $\overline{Nu}/\overline{Nu}_0$ data at a tested $Re(Re_a)$ decreases as Ta increases. The increase of $Re(Re_a)$ at any selected Ta produces a systematic reduction of $\overline{Nu}/\overline{Nu}_0$. In other words, the exponent of Re in the zero-buoyancy $\overline{Nu}_0$ correlation is not followed by the rotational heat transfer results so that the $\overline{Nu}/\overline{Nu}_0$ at a fixed Ta but different Re can not be converged in Fig. 10. Ta and Re are interdependent to affect $\overline{Nu}/\overline{Nu}_0$ in the manner of decreasing $\overline{Nu}/\overline{Nu}_0$ by way of increasing Ta and/or Re. Justified by each Ta driven data trend reveled in Fig. 10 at the tested Re, the zero-buoyancy $\overline{Nu}/\overline{Nu}_0$ data is correlated by Eq. (5) in which the correlative coefficients C_1, C_2 and C_3 are functions of Re.

$$C = C_1\{Re\} + C_2\{Re\} \times Ta + C_3\{Re\} \times Ta^2 \tag{5}$$

After reviewing the varying trends of C_s coefficients in Eq. (5) against Re, these C_s coefficients show the asymptotic varying trends and are accordingly correlated by (Eqs. (6)–(8)).

$$C_1 = 0.537 + 0.352 \times e^{-6.88E-5 \times Re} \tag{6}$$

$$C_2 = -2.19 \times 10^{-8} - 6.52 \times 10^{-8} \times e^{-1.07E-4 \times Re} \tag{7}$$

$$C_3 = 7.8 \times 10^{-16} + 5 \times 10^{-15} \times e^{-9.5E-5 \times Re} \tag{8}$$

D coefficient in Eq. (4) features the buoyancy impact on heat transfer. The positive (negative) sign of D coefficient reflects the improving (impeding) Gr_ω effect on $\overline{Nu}$. The larger (smaller) magnitude of D coefficient indicates the greater (lesser) degree of buoyancy impacts. For the entire parametric conditions examined here, all the D coefficients remain as positive but decreases as Ta increases for each Re tested. The improving buoyancy effects on heat transfer are weakened at the larger Ta. Interdependency of $\overline{Nu}$ on Ta and Gr_ω is demonstrated. It is also noticed that, at any fixed Ta, the increase of Re incurs a systematic increase in D values, in particular

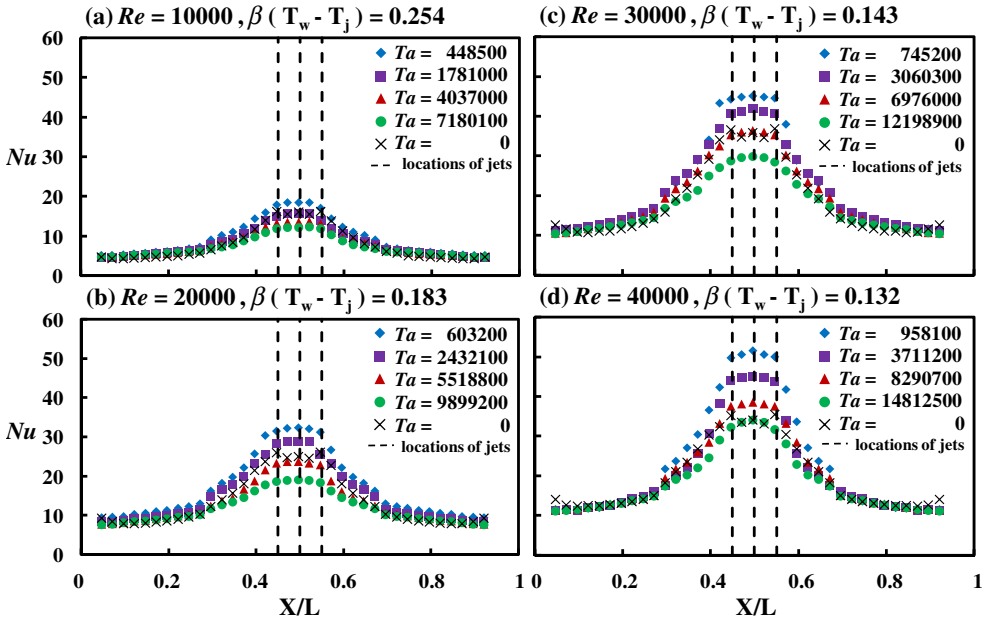

Fig. 8. Axial Nu distributions with five Ta at a nominal buoyancy level with (a) Re = 10000, (b) Re = 20000, (c) Re = 30000, (d) Re = 40000.

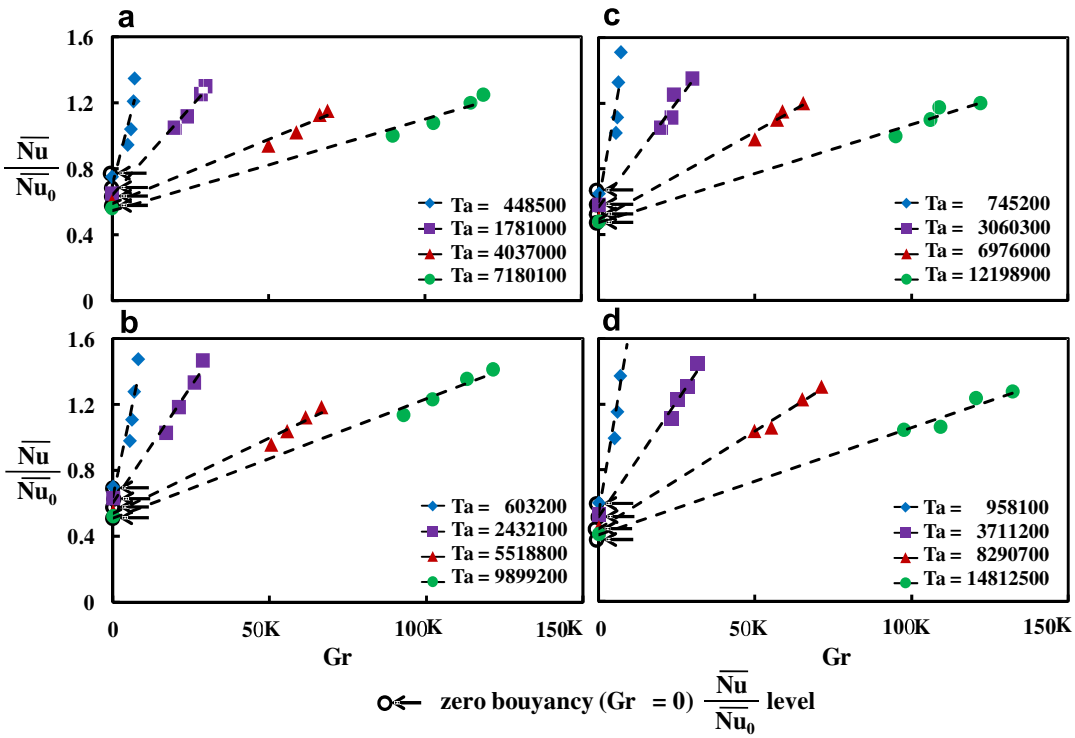

Fig. 9. Variations of $\overline{Nu}/\overline{Nu}_0$ against Gr_ω at four different Ta with (a) Re = 10000, (b) Re = 20000, (c) Re = 30000, (d) Re = 40000 demonstrating the extrapolating procedure to determine zero-buoyancy $\overline{Nu}/\overline{Nu}_0$ levels.

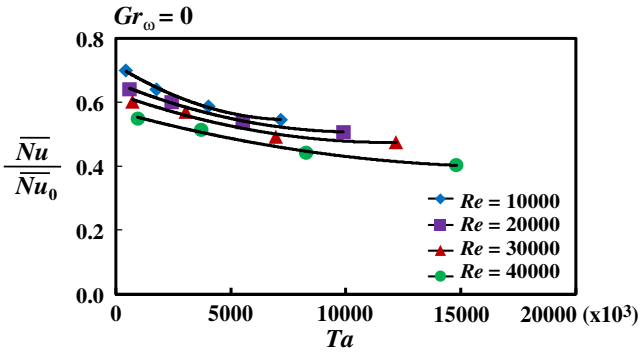

Fig. 10. Variations of $\overline{Nu}/\overline{Nu}_0$ at zero-buoyancy conditions against Ta at different Re.

with the parametric conditions of $Ta < 5 \times 10^6$. This demonstrates that the impacts of rotating buoyancy on heat transfer can be augmented by way of increasing Re. Nevertheless, $\overline{Nu}/\overline{Nu}_0$ correlation is formulated as Eq. (9) in which D_1, D_2 and D_3 are the correlative coefficients.

$$D = D_1\{Re\} + D_2\{Re\} \times e^{D3\{Re\}\times Ta} \tag{9}$$

D_s coefficients in Eq. (9) consistently decay asymptotically as Re increases. As a result, D_s correlations are derived as (Eqs. (10)–(12)).

$$D_1 = 9.26E-6 - 5.51E-6 \times e^{-4.94E-5\times Re} \tag{10}$$

$$D_2 = 2.05E-4 - 1.76E-4 \times e^{-5.47E-5\times Re} \tag{11}$$

$$D_3 = -5.92E-7 - 1.62E-6 \times e^{-1.18E-4\times Re} \tag{12}$$

A set of $\overline{Nu}/\overline{Nu}_0$ correlations that permits the evaluation of the interdependent or individual Re, Ta and Gr_ω effects on $\overline{Nu}/\overline{Nu}_0$ is derived by substituting C, D coefficients into Eq. (4). The overall success of this set of $\overline{Nu}/\overline{Nu}_0$ correlation is examined by comparing the calculated and experimental results in terms of $\overline{Nu}/\overline{Nu}_0$ and $\overline{Nu}$ as depicted in Fig. 11a and b, respectively. The maximum discrepancy of ±20% between the experimental and correlating results is achieved for 95% of the entire data generated. As revealed in Fig. 11a for the entire heat transfer data generated, the combined Re, Ta and Gr_ω effects have led the $\overline{Nu}/\overline{Nu}_0$ ratios in the range of 0.75–1.48. The $\overline{Nu}$ values in the present parametric conditions fall between 7.5 and 28, which corresponds to 30–112 if the characteristic length scale is alternatively defined as the height of the concentric annulus. Clearly, in the Re_a range of 600–2400 examined here, the heat transfer levels on the outer cylinder with the impinging jet-array issued from the rotating inner cylinder are considerably elevated from those achieved by the conventional annulus flows. This set of heat transfer correlations can be treated as a design reference for the present flow configuration. But, most importantly, the methodology devised by this study which can attack such complex heat transfer problems involving the interdependencies of Re, Ta and Gr_ω on $\overline{Nu}$ is applicable for other rotating jet-array geometries with cooling applications to the electric rotor machineries.

4. Conclusions

This experimental study investigates the heat transfer characteristics of an impinging jet-array issuing from the rotating inner cylinder in the concentric annulus with cooling applications to electric rotor machines. The following concluding remarks emerge from this study.

1. As Re increases, $\overline{Nu}_0$ increases accordingly and the axial span of each stagnation high Nu_0 region extends. As Gr_g increases, $\overline{Nu}_0$ decreases with the ranges of stagnation regions reduced. The higher degrees of Gr_g impacts develop at the stagnation region. Away form the stagnation region in both axial and angular

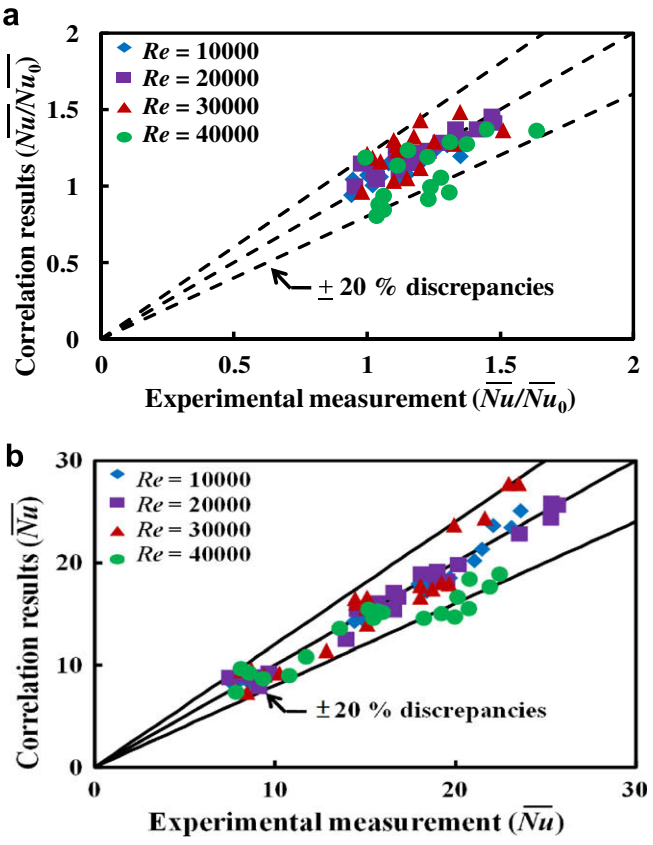

Fig. 11. Comparisons of correlation results with experimental data for (a)$\overline{Nu}/\overline{Nu}_0$, (b) $\overline{Nu}$.

directions; the effects of entraining hot spent-fluids into the cold jets; which phenomenon triggers the attendant Gr_g impacts are systematically faded.

2. Regression analyses for $\overline{Nu}_0$ revealed in Fig. 6 demonstrate the amplified Gr_g impacts on heat transfer as Re increases. With the consideration of such interdependency of Re and Gr_g on $\overline{Nu}_0$, the empirical $\overline{Nu}_0$ correlation is derived as Eq. (3) for present flow configuration.
3. A rather uniform Nu distribution over the stagnation region in contrast to the zigzag pattern for steady-jets is consequently developed over the impinging outer cylinder when the jet-array is issued from the rotating inner cylinder.
4. The impairing Gr_g effects on Nu_0 are reversed to improve heat transfer by increasing Gr_ω when the inner cylinder rotates. Locations where the Gr_g effects are most evident still develop in the stagnation regions with rotating inner cylinder. Away from the stagnation regions, the rotating buoyancy effects are gradually faded.
5. With all the rotating conditions examined here, local Nu and area-averaged $\overline{Nu}$ decrease as Ta increases. The present parametric conditions in terms of $Re(Re_a)$ and Ta fall in the ranges where the intermittences of jets and spent flows impede heat transfer performances from the steady-jet ones.
6. The heat transfer correlation derived as Eq. (5) takes into the account of the interdependent Re, Ta and Gr_g effects. The combined Re, Ta and Gr_g effects have led the $\overline{Nu}/\overline{Nu}_0$ ratios in the range of 0.75–1.48. Heat transfer levels from the conventional annulus flows in the Re_a range of 600–2400 are considerably elevated by using this newly devised cooling measure with the impinging jet-array issued from the inner rotating cylinder.

References

[1] G.I. Taylor, Stability of a viscous liquid contained between two rotating cylinders, Proc. Roy. Soc. London A 223 (1923) 289–343.
[2] K. Kataoka, Taylor vortices and instabilities in circular Couette flows, in: N.P. Cheremisinoff (Ed.), Encyclopedia of Fluid Mechanics, vol. 1, Gulf Publisher, Houston, TX, 1986, pp. 236–274. Chapter 9.
[3] M. Rudolph, T. Shinbrot, R.M. Lueptow, A model of mixing and transport in wavy Taylor–Couette flow, Phys. D 121 (1998) 163–174.
[4] N. Ohmura, T. Makino, A. Motomura, Y. Shibata, K. Kataoka, Intercellular mass transfer in wavy/turbulent Taylor vortex flow, Int. J. Heat Fluid Flow 19 (1998) 159–166.
[5] J. Chen, J. Kuo, The linear stability of steady circular Couette flow with a small radial temperature gradient, Phys. Fluids A 2 (1990) 1585–1591.
[6] R. Kedia, M.L. Hunt, T. Colonius, Numerical simulation of heat transfer in Taylor–Couette flow, ASME J. Heat Transfer 120 (1998) 65–71.
[7] H.A. Snyder, Experiments on the stability of spiral flow at low axial Reynolds numbers, Proc. Roy. Soc. London A 265 (1962) 198–214.
[8] M.A. Teamah, Numerical simulation of double diffusive laminar mixed convection in a horizontal annulus with hot, solutal and rotating inner cylinder, Int. J. Therm. Sci. 46 (2007) 637–648.
[9] R.C. Giordano, R.L.C. Giordano, D.M.F. Prazers, C.L. Cooney, Analysis of a Taylor–Poiseuille vortex flow reactorI: Flow patterns and mass transfer characteristics, Chem. Eng. Sci. 53 (1998) 3635–3652.
[10] S.T. Wereley, R.M. Lueptow, Velocity field for Taylor–Couette flow with an axial flow, Phys. Fluids 11 (1999) 3637–3649.
[11] D.I. Takeuchi, D.F. Jankowski, A numerical and experimental investigation of the stability of spiral Poiseuille flow, J. Fluid Mech. 102 (1981) 101–126.
[12] N.-S. Liu, X.-Y. Lu, Large eddy simulation of turbulent flows in a rotating concentric annular channel, Int. J. Heat Fluid Flow 26 (2005) 378–392.
[13] C.C. Wan, J.E.R. Coney, An experimental study of adiabatic spiral vortex flow, Int. J. Heat Fluid Flow 3 (1982) 31–38.
[14] T.M. Jeng, S.C. Tzeng, C.H. Lin, Heat transfer enhancement of Taylor–Couette–Poiseuille Flow in an annulus by mounting longitudinal ribs on the rotating inner cylinder, Int. J. Heat Mass Transfer 50 (2007) 81–390.
[15] A.M. Huber, R. Viskanta, Effect of jet-to-jet spacing on convective heat transfer to confined, impinging arrays of axisymmetric air jets, Int. J. Heat Mass Transfer 37 (1994) 2859–2869.
[16] L.M. Su, S.W. Chang, Detailed heat transfer measurements of impinging jet arrays issued from grooved surface, Int. J. Therm. Sci. 41 (2002) 823–841.
[17] B.R. Hollworth, L. Dagan, Arrays of impinging jets with spent fluid removal through vent holes on the target surface – Part I: average heat transfer, ASME J. Eng. Power 102 (1980) 994–999.
[18] A.I. Behbahani, R.J. Goldstein, Local heat transfer to staggered arrays of impinging circular air jets, ASME J. Eng. Power 105 (1983) 354–360.
[19] Y. Pan, B.W. Webb, Heat transfer characteristics of arrays of free-surface liquid jets, ASME J. Heat Transfer 117 (1995) 878–883.
[20] L.B.Y. Aldabbagh, I. Sezai, Three-dimensional numerical simulation of an array of impinging laminar square jets with spent fluid removal, Int. J. Therm. Sci. 43 (2004) 241–247.
[21] L.W. Florschuetz, R.A. Berry, D.E. Metzger, Periodic streamwise variation of heat transfer coefficients for inline and staggered arrays of circular jets with crossflow of spent air, ASME J. Heat Transfer 102 (1980) 132–137.
[22] L.W. Florschuetz, D.E. Metzger, C.C. Su, Y. Isoda, H.H. Tseng, Heat transfer characteristics for jet array impingement with initial crossflow, ASME J. Heat Transfer 106 (1984) 34–41.
[23] N. Obot, T.A. Trabold, Impingement heat transfer within arrays of circular jets. part I: effects of minimum, intermediate, and complete crossflow for small and large spacings, ASME J. Heat Transfer 109 (1987) 872–879.
[24] A.M. Huber, R. Viskanta, Convective heat transfer to a confined impinging array of air jets with spent air exits, ASME J. Heat Transfer 116 (1994) 570–576.
[25] Y. Huang, S.V. Ekkad, J.C. Han, Detailed heat transfer distributions under an array of orthogonal impinging jets, AIAA J. Thermophys. Heat Transfer 12 (1998) 73–79.
[26] K. Garrett, B.W. Webb, The effect of drainage configuration on heat transfer under an impinging liquid jet array, ASME J. Heat Transfer 121 (1999) 803–810.
[27] M. Rady, E. Arquis, Heat transfer enhancement of multiple impinging slot jets with symmetric exhaust ports and confinement surface protrusions, Appl. Therm. Eng. 26 (2006) 1310–1319.
[28] H.S. Sheriff, D.A. Zumbrunnen, Local and instantaneous heat transfer characteristics of arrays of pulsating jets, ASME J. Heat Transfer 121 (1999) 341–348.
[29] E.-C. Mladin, D.A. Zumbrunnen, Alterations to coherent flow structures and heat transfer due to pulsations in an impinging air-jet, Int. J. Therm. Sci. 39 (2000) 236–248.
[30] D.A. Zumbrunnen, M. Aziz, Convective heat transfer enhancement due to intermittency in an impinging jet, ASME J. Heat Transfer 115 (1993) 91–98.
[31] C. Gau, C.M. Chung, Surface curvature effect on slot-air jet impingement cooling flow and heat transfer process, ASME J. Heat Transfer 113 (1991) 858–864.
[32] G. Yang, M. Choi, J.S. Lee, An experimental study of slot jet impingement cooling on concave surface: effects of nozzle configuration and curvature, Int. J. Heat Mass Transfer 42 (1999) 2199–2209.

[33] N. Kayansayan, S. Küçüka, Impingement cooling of a semi-cylindrical concave channel by confined slot-air-jet, Exp. Therm. Fluid Sci. 25 (2001) 383–396.
[34] H. Eren, B. Yesilata, N. Celik, Nonlinear flow and heat transfer dynamics of impinging jets onto slightly-curved surfaces, Appl. Therm. Eng. 27 (2007) 2600–2608.
[35] Editorial Board of ASME Journal of Heat Transfer, Journal of heat transfer policy on reporting uncertainties in experimental measurements and results, ASME Journal of Heat Transfer 115 (1993) 5–6.
[36] V. Gilard, L.E. Brizzi, Slot jet impinging on a concave curved wall, ASME J. Fluids Eng. 127 (2005) 595–603.